Research Article

Nano Research
2020, 13(11): 3130–3136

ISSN 1998-0124 CN 11-5974/O4
https://doi.org/10.1007/s12274-020-2983-6

Morphology and strain control of hierarchical cobalt oxide nanowire electrocatalysts via solvent effect

Xiuming Bu[1,2,§], Xiongyi Liang[1,§], Kingsley O. Egbo[2], Zebiao Li[1], You Meng[1], Quan Quan[1], Yang Yang Li[1], Kin Man Yu[2], Chi-Man Lawrence Wu[1] (✉), and Johnny C. Ho[1,3] (✉)

[1] *Department of Materials Science and Engineering, City University of Hong Kong, Kowloon, Hong Kong SAR, China*
[2] *Department of Physics, City University of Hong Kong, Kowloon, Hong Kong, Kowloon, Hong Kong SAR , China*
[3] *State Key Laboratory of Terahertz and Millimeter Waves, City University of Hong Kong, Kowloon, Hong Kong SAR, China*
[§] *Xiuming Bu and Xiongyi Liang contributed equally to this work.*

Received: 30 April 2020 / **Revised:** 25 June 2020 / **Accepted:** 12 July 2020

ABSTRACT

Designing highly efficient and low-cost electrocatalysts for oxygen evolution reaction is important for many renewable energy applications. In particular, strain engineering has been demonstrated as a powerful strategy to enhance the electrochemical performance of catalysts; however, the required complex catalyst preparation process restricts the implementation of strain engineering. Herein, we report a simple self-template method to prepare hierarchical porous Co_3O_4 nanowires (PNWs) with tunable compressive strain via thermal-oxidation-transformation of easily prepared oxalic acid-cobalt nitrate ($Co(NO_3)_2$) composite nanowires. Based on the complementary theoretical and experimental studies, the selection of proper solvents in the catalyst preparation is not only vital for the hierarchical structural evolution of Co_3O_4 but also for regulating their compressive surface strain. Because of the rich surface active sites and optimized electronic Co d band centers, the PNWs exhibit the excellent activity and stability for oxygen evolution reaction, delivering a low overpotential of 319 mV at 10 mA·cm^{-2} in 1 M KOH with a mass loading 0.553 mg·cm^{-2}, which is even better than the noble metal catalyst of RuO_2. This work provides a cost-effective example of porous Co_3O_4 nanowire preparation as well as a promising method for modification of surface strain for the enhanced electrochemical performance.

KEYWORDS

hierarchical structure, morphology control, compressive strain, solvent effect, oxygen evolution reaction

1 Introduction

Electrochemical water splitting into hydrogen and oxygen provides an efficient energy conversion technology to reduce the dependence on carbon-based fossil fuels as well as their negative impact on the environment [1, 2]. As compared with the two-electron transfer hydrogen evolution reaction (HER) at cathode, the oxygen evolution reaction (OER) is a four-electron process with the slower kinetics being a limiting factor for the further efficiency improvement of overall water splitting [3]. Thus, it is necessary to develop efficient non-noble metal and earth-abundant OER catalysts to lower the reaction energy barrier. Among many promising catalyst materials, transition metal oxides (TMOs) have recently gained a substantial attention because of their favorable electronic structures for the efficient intermediate binding to generate oxygen [4].

At the same time, because of the large surface-to-volume ratio, small crystal sizes and shortened ion diffusion length, one-dimensional (1D) porous nanowires (PNWs) together with their unique structure-dependent properties are recognized as one of the most promising materials for energy-related applications [5]. In general, PNWs can be obtained via the preparation of one-dimensional backbone followed by post- treatment process. Although there are several oxide (MnO_2 [6], Fe_2O_3 [7], Co_3O_4 [8]), nitride (VN [9], GaN [10]) and carbon-based PNW materials [11, 12] synthesized by various methods, such as electrospinning, template-assisted and chemical deposition, unfortunately, it is still challenging to prepare uniform PNWs in low cost with mild reaction conditions on account of the uncontrollable nucleation and growth during synthesis.

Except morphology engineering, various rational strategies are also extensively explored to manipulate the active sites of TMOs via different surface atomic coordination and arrangement [13–18]. To date, strain engineering has been recognized as one of the powerful methods to effectively modify the surface electronic structure of materials [19, 20]. The effect of strain engineering (tensile and compressive strain) on TMO catalysts can modulate their d band center positions in order to reduce the chemisorption potential energies or energy barriers [19, 21]. Currently, direct deposition of target materials on the structurally tunable substrates is the main preparation method to obtain the precisely controlled and uniform surface strain on the catalysts. For instance, strained MoS_2 monolayers have been prepared on the Au nanocone arrays via vapor deposition. Subsequent experiments and density functional theory (DFT) calculations further confirmed that the hydrogen adsorption free energy of MoS_2 could be manipulated by controlling the surface strain [22]. In the case of TMOs, oxygen-vacancy-rich

Address correspondence to Chi-Man Lawrence Wu, lawrence.wu@cityu.edu.hk; Johnny C. Ho, johnnyho@cityu.edu.hk or johnnyho99@gmail.com

CoO nanorods with a tensile strain of 3% were prepared by using ZnO nanorods as the ion exchange template, resulting in the appropriate H adsorption on the {111} surface because of the enhanced covalency of Co-O bands, and further achieving the excellent electrochemical activity [23]. Although all these surface strained catalysts with the impressive electrocatalytic performance is beneficial for fundamental studies investigating relationships between the strain and the electrochemical properties, it is still unfortunately challenging to prepare catalysts with controlled surface strain surface by cost-effective chemical reactions under mild conditions.

In this work, we propose and achieve a simple self-template strategy to prepare porous Co_3O_4 NWs (PNWs) through thermal oxidation of cost-effective and easily prepared Co-oxalic dodecahedron in air atmosphere. During careful investigation of the formation mechanism of PNWs, the ethanol content of precursor solutions is found to be vital for controlling the nucleation direction and morphology evolution of obtained Co_3O_4 PNWs. X-ray diffraction (XRD), ultraviolet photoemission spectroscopy (UPS) and thermogravimetric analysis (TGA) further reveal the obvious compressive strain appeared on the PNW surface due to the restriction effect of the Co-oxalic dodecahedron precursors and escape rate of carbon dioxide during the thermal treatment, which results in the upshift of d band center of Co, enhancing the intermediate adsorption. Originating from this unique porous 1D structure with compressive surface strain, these PNWs are then decorated with rich surface active sites, exhibiting the remarkable OER performance with a small overpotential of 319 mV at a current density of 10 $mA{\cdot}cm^{-2}$ in 1 M KOH electrolyte. The PNWs catalyst can also maintain an impressively stable operational performance for 15 h. All these findings do not only provide a promising route for the facile preparation of PNWs but also achieve a simple but effective scheme to manipulate the surface strain of materials.

2 Experimental

2.1 Preparation of porous cobalt oxide nanowires

Typically, 1 mM of $Co(NO_3)_2{\cdot}6H_2O$ and 1 mM of $H_2C_2O_4$ were dissolved in 10 mL of ethanol under magnetic stirring for 2 h to form a homogeneous solution. The prepared solution was then transferred to a 15 mL stainless-steel Teflon-lined autoclave. Next, the autoclave was sealed and heated in an electric oven at 180 °C for 12 h. The obtained precipitation was washed with ethanol several times and dried at 60 °C overnight under vacuum. Finally, the Co_3O_4 nanostructures were obtained via thermal treatment at 400 °C with a heating rate of 10 $°C{\cdot}min^{-1}$ for 2 h in air atmosphere. For comparison, notably, utilizing the above-described method, Co_3O_4 nanostructures with different morphologies could be prepared by replacing the ethanol solution with the mixed solution of distilled water and ethanol (i.e., V_{H_2O}:V_{EtOH} = 10:0, 7:3, 5:5, 3:7). For comparison, the porous Co_3O_4 nanowires treated with different heating rates of 5 and 15 $°C{\cdot}min^{-1}$ were also prepared.

2.2 Material characterization

Crystalline structure of the prepared samples was evaluated by powder XRD using a scanning rate of 0.05 $°{\cdot}s^{-1}$ in a 2θ scan ranging from 10° to 90°, employing a Bruker D2 Phaser (Bruker, Billerica, MA, USA) instrument equipped with the monochromatized Cu–Kα radiation. The TGA curves were obtained by TGA (SDT Q600) from 25 to 500 °C at a heating rate of 10 $°C{\cdot}min^{-1}$ in air atmosphere. Field-emission scanning electron microscope (FESEM, SU-8010, Hitachi, Tokyo, Japan) with an accelerating voltage of 15 kV as well as transmission electron microscopy (TEM) and high-resolution TEM (HRTEM) conducted by a Tecnai G^2 F30 (FEI, Hillsboro, OR, USA) using an accelerating voltage of 300 kV were performed to observe the morphologies and dimensions of the samples. Brunauer-Emmett-Teller (BET) specific surface area and pore volume of the samples were assessed based on nitrogen adsorption isotherms using a NOVA 1200e gas adsorption apparatus (Quantachrome Instruments, Boynton Beach, FL, USA). X-ray photoelectron spectroscopy (XPS) was recorded with a VG Multilab 2000 (Thermo Fisher Scientific, Waltham, MA, USA) photoelectron spectrometer using the monochromatic Al–Kα radiation under vacuum at a pressure of 2×10^{-6} Pa. All the binding energies were referenced to the C 1s peak at 284.8 eV of the surface adventitious carbon. The valence band spectra were determined by UPS. Measurements were conducted using a KP technology (APS04) instrument in an N_2-filled APS module and Faraday enclosure. The Kelvin probe tip (2 mm in diameter) was calibrated using a highly oriented pyrolytic graphite (HOPG) standard. In the UPS measurement, the samples are illuminated with a 4–5 mm diameter of light spot from a tunable monochromated D2 lamp.

2.3 Electrochemical measurement

All electrochemical characterization were investigated with a Gamry 300 electrochemical workstation with a three-electrode system at room temperature. To prepare the working electrode, 5 mg of electrocatalysts (as-synthesized samples) were ultrasonically dispersed in a mixed solution containing 100 μL of deionized (DI) water, 340 μL of ethanol and 20 μL of Nafion (5 wt.%) for 2 h to obtain a uniform suspension. Then, 10 μL of electrocatalyst ink was drop-casted onto the polished glassy carbon electrode with a diameter of 5 mm, in which the mass loading was found to be about 0.553 $mg{\cdot}cm^{-2}$. The prepared electrode was next dried at ambient condition overnight. A saturated Ag/AgCl electrode and a carbon rod were employed as the reference electrode and counter electrode, respectively. All potentials reported in this work were calibrated versus the reversible hydrogen electrode (RHE) using an equation of $E_{RHE} = E_{SCE} + (0.197 + 0.059 \times pH)$ V, where E_{RHE} is the potential referred to RHE and E_{SCE} is the measured potential against the saturated calomel electrode (SCE) reference electrode. The OER activity was measured in 1 M KOH (pH = 13.73) by linear sweep voltammetry (LSV) at a scan rate of 5 $mV{\cdot}s^{-1}$. Before testing, 10 cyclic voltammetry (CV) cycles were conducted until the redox peaks and the oxygen evolution currents showed the unobvious change. Unless otherwise mentioned, the voltammograms were recorded with the iR drop compensation automatically performed on the workstation. To calculate the turnover frequency (TOF) values, we employed the previously reported calculation method [24]

$$\mathrm{TOF} = \frac{j \times A_{ox}}{4 \times e \times N_A}$$

where j is the current density, A_{ox} is the total surface area on the GC electrode, e is the electric charge carried by a single electron, N_A is the number of the Co atoms. Here, only the Co atoms from the outmost surface is considered. Since the cubic Co_3O_4 structure is mainly dominated by the (311) surface, the lattice parameters of $a = b = c = 8.065$ Å are used while the (311) surface are examined. The Co density along the (311) surface can then be determined as $16/(10.69 \times 10^{-10} \times$

18.51×10^{-10}) ~ 8.09×10^{18} atom·m^{-2}, considering 16 Co atom sitting in this crystal plane in the cell.

2.4 Computational methods

All the first principle calculations were performed using plane-wave DFT as implemented in Quantum Espresso [25, 26]. Generalized gradient approximation (GGA) with Perdew-Burke-Ernzerhof (PBE) functional was selected to describe the exchange-correlation interaction [27]. Van der Waals interactions were considered using the Grimme's DFT-D3 method [28]. A plane-wave cutoff of 60 Ry and a density cutoff of 480 Ry were used based on standard solid state pseudopotentials with projector augmented-wave (PAW) method [29, 30]. For sampling the Brillouin zone, Monkhorst-Pack k-point was set as 3 × 3 × 3, while a larger 6 × 6 × 6 k-point was used to investigate the electronic properties. All atoms were fully relaxed until the forces on each atom being less than 0.02 eV·Å^{-1}. The effects of strain, ε, on the electronic properties of Co_3O_4 were studied, where the strain is defined as the ratio of deformation, Δa, to the initial lattice constant of Co_3O_4, a_0 (i.e., $\varepsilon = \Delta a/a_0$).

3 Results and discussion

Here, porous Co_3O_4 nanowires were synthesized simply through thermal oxidation of $Co(NO_3)_2$ and oxalic acid in the ethanol solution to yield Co-oxalic dodecahedron (Co-Ox) nanostructures, followed by the thermal treatment in air atmosphere. It is noted that all precursors, including oxalic acid, are commonly used low-cost chemicals employed in both laboratory and industry. The morphologies of obtained Co-Ox precursors were characterized by scanning electron microscope (SEM). As shown in Fig. S1 in the Electronic Supplementary Material (ESM), it is clear that the obtained Co-Ox nanostructures are highly uniform with a diameter of ~ 70 nm and a length of up to several micrometers. Figures 1(a) and 1(b) give the TEM images of the final product of Co_3O_4 PNWs, in which there are uniform nanowires with rough surface decorated with nanoparticles. Also, there are numerous amounts of voids existed between nanoparticles, which are resulted from the volume reduction induced by the precursor pyrolysis. These voids can increase the exposed area of active sites, which ensure the effective contact between electrolyte and catalyst surface, facilitating efficient charge and mass transfer through the electrode-electrolyte interface [31]. At the same time, as depicted in the high-resolution TEM image in the inset of Fig. 1(b), there are lattice fringes clearly observed with a spacing of 0.24 nm, which corresponds to the (311) crystal planes of Co_3O_4 [32].

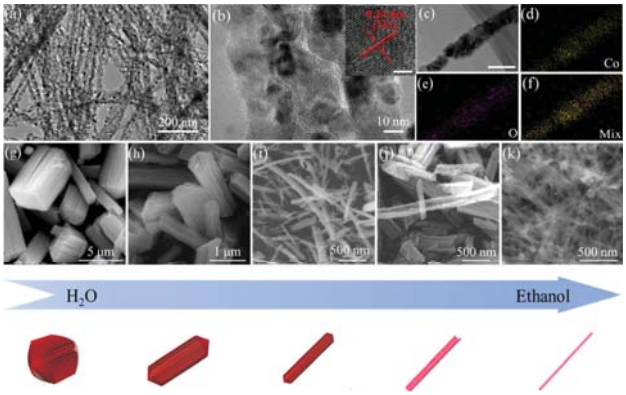

Figure 1 (a) TEM and (b) HRTEM images of porous Co_3O_4 nanowires. (c)–(f) Element mappings of a typical porous Co_3O_4 nanowire. SEM images of illustrating the hierarchical structure evolution of Co_3O_4 together with their corresponding structure models when the solvent has the following volume ratio of H_2O:EtOH: (g) 1:0; (h) 7:3; (i) 5:5; (j) 3:7 and (k) 0:1.

Combined with the uniform distribution of constituent elements (i.e., Co and O) as presented in the chemical mappings in Figs. 1(c)–1(f), it is evident that porous Co_3O_4 nanowires are successfully fabricated through a simple wet chemistry scheme here.

To shed light into the formation mechanism of porous Co_3O_4 nanowires, the hierarchical structural evolution of Co_3O_4 were thoroughly evaluated by SEM together with the corresponding structure models as illustrated in Figs. 1(g)–1(k). By simply controlling the solvent volume ratio of water to ethanol to 1:0, 7:3, 1:1, 3:7 and 0:1, five different kinds of hierarchical morphologies of Co_3O_4, i.e., microparticles, nanopillars, nanorods, nanotubes and nanowires, were obtained. Specifically, when only deionized water is served as the solvent, large hierarchical Co_3O_4 microparticles (around 5 μm in diameter) were formed that composed of plate shaped lamina features (Fig. 1(g)). Once ethanol was introduced with its increasing volume concentration, the size of the hierarchical structure decreased substantially, while the aspect ratio between the length and the width of Co_3O_4 increased. For example, hierarchical Co_3O_4 nanopillars and nanorods were prepared when the volume ratio of water to ethanol is 7 to 3 and 1 to 1, respectively (Figs. 1(h) and 1(i)). After the ratio of water to ethanol continued to decrease, reaching 3 to 7, uniform Co_3O_4 nanotubes were achieved (Fig. 1(j)). Eventually, as soon as ethanol was served as the only solvent, the morphology of Co_3O_4 was entirely changed from nanotubes to nanowires (Fig. 1(k)). Based on these comparative experiments, it is obvious that the choice of solvents used in the hydrothermal reaction plays a key role on the morphologies of obtained Co_3O_4 nanostructures. In detail, the nucleation and growth process of Co-Ox is anticipated to get suppressed with the increasing ethanol volume concentration in the reaction medium due to the larger viscosity, lower boiling point and lower dielectric constant of ethanol as compared with those of water. It is worth noting that ethanol would affect the formation of micelle structures through the interaction of metal with hydroxyl groups, dictating the structure-direction properties during the Ostwald ripening process of Co-Ox intermediates [33]. Therefore, this thermodynamic process induces the nanoparticle self-assembly into different morphologies under the guidance of ethanol. Five different hierarchical Co_3O_4 nanostructures (i.e., microparticles, nanopillars, nanorods, nanotubes and nanowires) assembled by sheet-like Co_3O_4 or nanoparticles can then be effectively obtained by just manipulating the ethanol volume concentration in the solvent. In general, when electrocatalysts are configured from bulk materials into porous nanowires, their device performances can be enhanced because of the larger surface-to-volume ratio and shortened ion and/or carrier diffusion length of NWs [34]. In this work, specific surface area and average pore size of these hierarchical Co_3O_4 samples were measured by BET and Barrett–Joyner–Halenda (BJH) methods, respectively. The BET analysis reveals that the porous Co_3O_4 nanowires have the largest surface area of 82.60 m^2·g^{-1} which is substantially larger than the ones of Co_3O_4 microparticles (9.44 m^2·g^{-1}), Co_3O_4 nanopillars (44.12 m^2·g^{-1}), Co_3O_4 nanorods (49.03 m^2·g^{-1}) and Co_3O_4 nanotubes (61.70 m^2·g^{-1}) (Fig. S2 in the ESM). At the same time, the measurement of average pore size shows the similar data trend (Fig. S3 in the ESM). The porous Co_3O_4 nanowires exhibit the largest pore volume (0.361 cc·g^{-1}) that is in a distinct contrast to those of Co_3O_4 microparticles (0.214 cc·g^{-1}), Co_3O_4 nanopillars (0.221 cc·g^{-1}), Co_3O_4 nanorods (0.237 cc·g^{-1}) and Co_3O_4 nanotubes (0.243 cc·g^{-1}). Both BET and BJH results confirm the largest active site surface area of Co_3O_4 PNWs which is beneficial for the electrochemical performance improvement as summarized in Table S1 in the ESM.

Apart from the morphological characterization, it is also important to evaluate the chemical composition of different hierarchical Co_3O_4 structures. Fourier transform infrared spectroscopy (FTIR) was then employed to assess the structural and composition information of Co-Ox precursors prepared with solvents with different volume concentration of ethanol in water (Fig. S4 in the ESM). In principle, the peak at 494 cm^{-1} reveals the existence of the Co-O band, while the peaks at 1,616 and 3,386 cm^{-1} are attributed to the C=C and –OH bands, indicating the coordination character of Co^{2+} with oxalic species [35]. It is clear that the similar FTIR curves are observed for all the samples, designating that the difference in solvents with various volume concentration of ethanol in water only changes the morphology but does not alter chemical composition of the product. Importantly, the TGA test under an air atmosphere exhibits a weight loss of 18 wt.% and 37 wt.% at 250 and 300 °C from the H_2O and organic components, respectively, for the nanowire sample (Fig. S5 in the ESM). The molecular formula of the Co-Ox nanowire precursor can be proposed to be Co(Oxalic)·$x$$H_2O$ based on the FTIR and TGA analysis. Also, X-ray diffraction (XRD) was used to investigate the crystal structure of the prepared samples. As shown in Fig. 2(a), the five different hierarchical Co_3O_4 samples have the similar XRD spectra, which are consistent with the cubic Co_3O_4 structure (JCPDS 74-1656). But there is an apparent difference existed in the low-angle region of the spectra, where the peaks at ~ 37° are observed to shift towards the larger angle with the increasing ethanol volume concentration in the reaction solvent (Fig. 2(b)). In particular, based on Bragg's law, the prominent reflection peaks located at 37.035° (Co_3O_4 microparticles), 37.103° (Co_3O_4 nanopillars), 37.126° (Co_3O_4 nanorods), 37.144° (Co_3O_4 nanotubes) and 37.304° (Co_3O_4 PNWs) are corresponded to the interlayer spacings of 2.4254, 2.4211, 2.4196, 2.4185, and 2.4085 Å, respectively [36]. This decreased interlayer spacing of the (311) crystal planes indicates the existence of compressive strain on the catalyst. These compressive strains can be calculated via the analytical equation of $\varepsilon = ((a_{prepared} - a_{reference})/a_{reference}) \times 100\%$, where ε is the lattice strain, $a_{prepared}$ and $a_{reference}$ represent the lattice parameters of the prepared and reference catalysts, respectively [19]. The reference catalyst is referred to the one with the lattice parameter calculated from the peak value in standard JCPDS card 74-1656. Figure 2(c) summarizes the results, in which the compressive strain of Co_3O_4 microparticles, Co_3O_4 nanopillars, Co_3O_4 nanorods, Co_3O_4 nanotubes and Co_3O_4 PNWs are found to be 2.74±0.30%, 3.73±0.30%, 4.07±0.28%, 4.32±0.26% and 6.61±0.28%, respectively.

During the conversion process from Co-Ox precursors to Co_3O_4 catalysts (Co-Ox → Co_3O_4 + CO_2 + H_2O), the crystal nucleation and growth of Co_3O_4 is seriously affected by the size of the precursor [37]. The smaller the size of the precursor, the greater the restriction on the crystal growth. In this case, restriction is the main source of strain. At the same time, the escape rate of carbon dioxide would affect the nucleation and growth rate of Co_3O_4 crystals (Fig. 2(d)). The TGA results illustrate that in all precursors, the weight ratio of H_2O (marked with blue dotted box) and CO_2 (marked with yellow dotted box) discharged is exactly the same, but the conversion time is different (Fig. 2(e)). The corresponding integration curve provides more detailed information that can be used to characterize the CO_2 escape rate (Fig. 2(f)). The sharper the peak, the higher the rate of carbon dioxide escape per unit time is observed. It is shown that the PNW precursor has the largest CO_2 escape rate, which can be attributed to its largest specific surface area. Therefore, the smallest precursor volume and the fastest carbon dioxide escape rate result in the largest compressive strain on the PNWs.

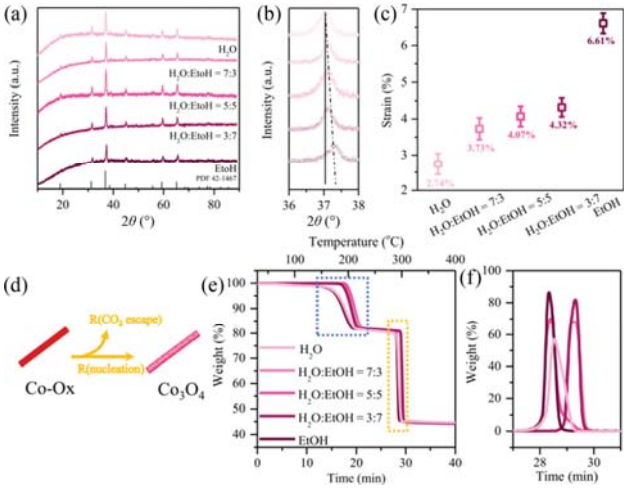

Figure 2 (a) XRD spectra and (b) the corresponding high-resolution low-angle region of 36°–38° of various hierarchical Co_3O_4 structures. (c) Summary of the lattice strain compiled for all the prepared samples. (d) Schematic diagram of stress formation, *R* is the abbreviation of rate. (e) TGA curves of the Co-Ox precursors and (f) is the corresponding integral curve in the range of 26–32 min.

In addition, XPS was utilized to assess the electronic structure of active sites of all the catalysts (Fig. 3(a)). It is noted that all the Co 2p spectra display two main peaks located at 778.6 and 794.7 eV, which can be assigned to Co $2p_{3/2}$ and Co $2p_{1/2}$, accordingly. The peak positions are nearly the same among all the samples, illustrating that there is not any electron transfer between Co and O atoms and no new chemical bonds or defects formed here. Importantly, the valence band spectra of obtained hierarchical Co_3O_4 catalysts were determined by UPS. As depicted in Fig. 3(b), the valance band values (vs. vacuum) are measured to be around −5.32, −5.39, −5.48, −5.53 and −5.62 eV for the catalysts prepared with the increasing ethanol volume concentration in the reaction solvent, respectively, demonstrating the upshift of valence band position due to the solvent effect. By just manipulating the solvent effect, the compressive strain and valence band position of the Co_3O_4 catalysts can be effectively controlled.

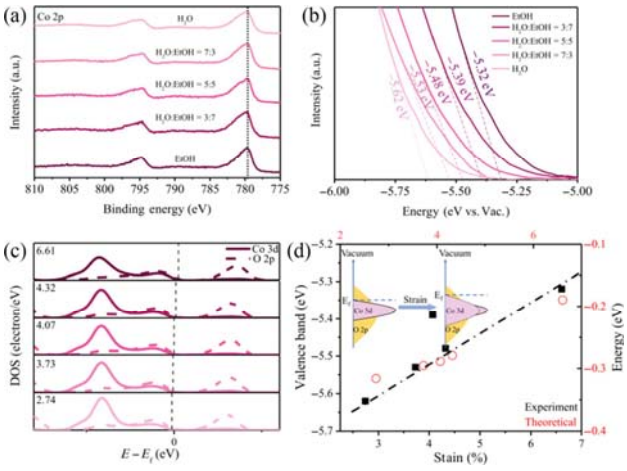

Figure 3 (a) High-resolution Co 2p XPS spectra and (b) UPS valance band spectra of various hierarchical Co_3O_4 structures. (c) Computed projected density of states of Co_3O_4 crystal with different compressive strain, ranging from 2.74% to 6.61%. (d) Theoretically calculated valence band position as a function of compressive strain applied on Co_3O_4 (vacuum level is 0). Inset of (d) is the schematic illustration of the effect of compressive strain on the energy band structure and crystal configuration of Co_3O_4.

Furthermore, DFT was carried out to study the possible effect of compressive strain on the energy band structure of prepared Co_3O_4 samples (Fig. S6 in the ESM). Figure 3(c) presents the changes of energy levels and their bandwidths of Co_3O_4 with different compressive strain. As the strain increases, the overlap of wave functions of the Co and O atoms enlarges, leading to the collection of Co 3d valence orbitals gradually broadened into bands, where the formed overlapped area with O 2p would further widen the bandwidth. In order to maintain the constant number of electrons in the valence band, the d band center of Co_3O_4 upshifts, which is reflected on the movement of dash line as illustrated in the inset of Fig. 3(d). The upshift of d band center would result in the enhanced interaction between the adsorbates and catalyst surface [21]. In a typical four-electron OER process occurred on the surface of transition metal oxides in alkaline conditions, the reaction begins with the adsorption of OH^- on the catalyst surface to form OH intermediates. Then, the OH intermediates react with free OH^- to produce adsorbed atomic O species, followed by the reaction of OH^- with adsorbed atomic O to form adsorbed OOH species. Eventually, the O_2 releases because of the reaction between the adsorbed OOH species and additional OH^- [37]. In general, the formation of adsorbed OOH species is often recognized as the rate determining step [38]. Therefore, the increased Co-O covalency and elevated computed d center relative to the Fermi level are beneficial for the OER activity improvement. Meanwhile, the theoretical values of valence band position were also obtained and observed to upshift with the increasing compressive strain (Fig. 3(d)), in which the results agree well with the above discussion. It is clear that the compressive strain can effectively manipulate the energy band structure of Co_3O_4 for the enhanced OER characteristics.

Besides the effect of compressive strain, the 1D structure and porous feature of hierarchical Co_3O_4 catalysts are anticipated to deliver the excellent electrochemical performance. In this case, electrochemical activities of the five different hierarchical Co_3O_4 samples were investigated towards OER by recording iR-corrected polarization curves using a representative three-electrode configuration in 1 M KOH electrolyte. The polarization curves of these five hierarchical Co_3O_4 catalysts deposited on glassy carbon electrodes with a mass loading of about 0.553 mg·cm^{-2} are depicted in Fig. 4(a). For a fair comparison purpose, commercial Ru_2O catalysts were also evaluated and presented in the polarization curves. Among the five Co_3O_4 electrodes, hierarchical Co_3O_4 PNWs demonstrate the best OER performance with an overpotential of 319 mV at 10 mA·cm^{-2}, which is better than the ones of Co_3O_4 microparticles (432 mV), Co_3O_4 nanopillars (353 mV), Co_3O_4 nanorods (347 mV) and Co_3O_4 nanotubes (340 mV). It is also worth mentioning that the OER current of Co_3O_4 PNWs exceeds the commercial Ru_2O particles when the applied potential is lager than 1.58 V (vs. RHE), since the special 1D PNWs structure can facilitate the more efficient electron and mass transport during the period of high current densities. These impressive results are already better than other state-of-the-art Co_3O_4 nanostructures reported in recent literatures and even competable to other transition metal oxide catalysts (Table S2 in the ESM). The OER kinetic characteristics of these electrodes were next investigated via Tafel slopes [39]. As given in Fig. 4(b), Co_3O_4 PNWs have the smallest Tafel slope of about 51 mV·dec^{-1}, where this slope is significantly smaller than that of Co_3O_4 microparticle (71 mV·dec^{-1}), Co_3O_4 nanopillars (65 mV·dec^{-1}), Co_3O_4 nanorods (56 mV·dec^{-1}) and Co_3O_4 nanotubes (54 mV·dec^{-1}), also being smaller than the one of commercial RuO_2 catalysts (68 mV·dec^{-1}). All these findings can evidently confirm the superior intrinsic OER properties of Co_3O_4 PNWs [40]. Obviously, the catalyst morphology is anticipated to have a significant influence on the OER activity. In order to confirm the important contribution of compressive strain to the electrocatalytic performance, various samples of Co_3O_4 PNWs were prepared with different heating rates of 5, 10, and 15 °C·min^{-1} (Fig. S7 in the ESM). Based on the above analysis, the higher heating rate would lead to the higher CO_2 escape rate, thus improving the strain applied to the samples. The XRD results further prove that the samples prepared with different heating rates do indeed have different degrees of strain (Fig. S8 in the

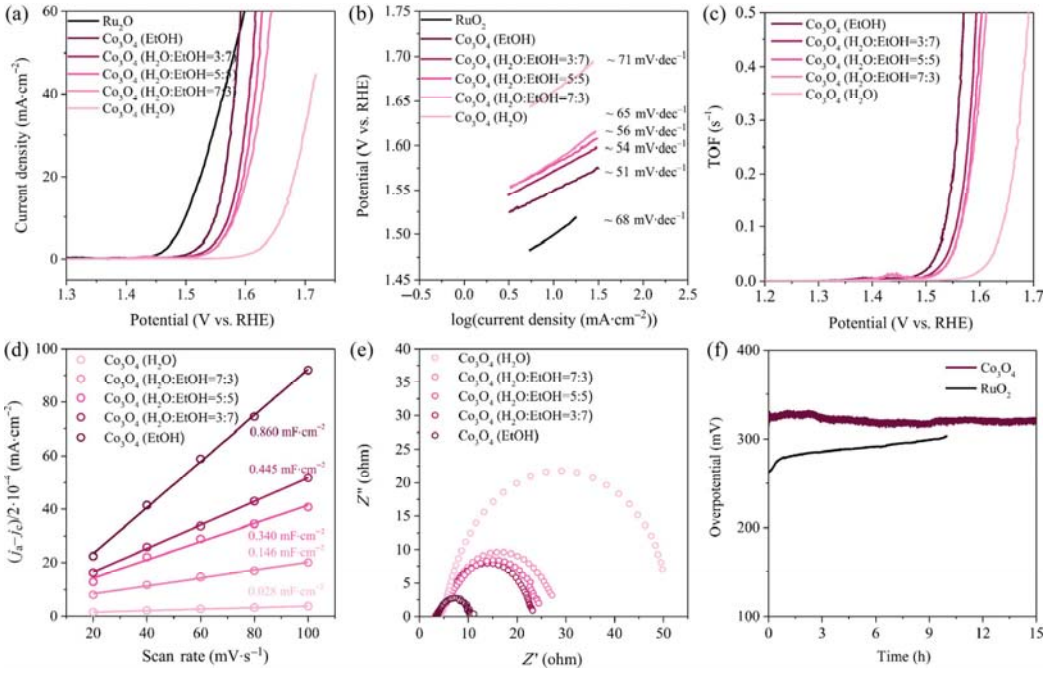

Figure 4 (a) LSV curves of the five different kinds of hierarchical Co_3O_4 structures and commercial RuO_2. (b) Corresponding Tafel plots. (c) The potential dependent TOF plots for these hierarchical Co_3O_4 structures. (d) ECSA-normalized polarization curves. (e) Nyquist plots of different Co_3O_4 catalysts. (f) Current-time curves recorded in a potentiostatic electrolysis experiment.

ESM). The polarization curves of these three samples indicate the Co_3O_4 PNWs prepared with 10 °C·min^{-1} having the best OER performance (Fig. S9 in the ESM). These results not only confirm the key factor of strain in the electrocatalytic activity, but also reveal the strain optimization is essential during the catalyst material design process. In addition, to quantitatively evaluate the intrinsic activity for each catalytic site, the TOF values were calculated and compiled in Fig. 4(c) (see calculation details in Experimental Section). The TOF value of Co_3O_4 microparticles was only 0.002 s^{-1} at the overpotential of 300 mV versus RHE, while the corresponding TOF value of Co_3O_4 PNWs is 0.194 s^{-1}, clearly indicating that the coordinated control of morphology and strain can intrinsically improve the essential catalytic activity of Co_3O_4.

Moreover, the electrochemical double-layer capacitance (C_{dl}) measured via CV was used to assess the electrochemical active surface areas (ECSA) of prepared catalysts as shown in Fig. S10 in the ESM, where C_{dl} is considered to be directly proportional to the catalyst's effective surface area [41]. This way, CVs with the increasing scanning rates were measured in the non-Faradaic region (0.05–0.1 V vs. Ag/AgCl) for these electrodes. C_{dl} values are then obtained to be around 0.860, 0.445, 0.340, 0.146 and 0.028 mF·cm^{-2} for the catalysts of Co_3O_4 PNWs, Co_3O_4 nanotubes, Co_3O_4 nanorods, Co_3O_4 nanopillars and Co_3O_4 microparticles, respectively (Fig. 4(d)). These results indicate that Co_3O_4 PNWs have the largest active surface area that is consistent with the conclusion from the overpotential and Tafel slope analysis. At the same time, ECSA-normalized polarization curves of different Co_3O_4 catalysts were compiled in order to reflect the intrinsic activities of catalysts (Fig. S11 in the ESM). It is observed that the calculated overpotentials follow the same data trend as Fig. 4(a), indicating the intrinsic activity of Co_3O_4 PNWs being superior than others due to the full exposure of active sites and optimized d band center. To further evaluate OER kinetics at the interface between electrode and electrolyte, electrochemical impedance spectroscopy (EIS) was conducted at 0.6 V (vs. Ag/AgCl) [40]. The EIS results show the reduced charge transfer resistance (R_{ct}) with the increasing volume concentration of ethanol in water in the reaction solvent, inferring the hierarchical Co_3O_4 PNWs with the fastest charge transfer process here (Fig. 4(e)) [42]. The long-term durability tests of Co_3O_4 PNWs were also measured via chronopotentiometry (V–t) at a constant current density of 10 mA·cm^{-2} in 1 M KOH, in which there is only a little decay in the performance over 15 h of continuous operation (Fig. 4(f)), exceeding the performance of commercial Ru_2O. All these apparently demonstrate the excellent electrochemical OER performance of hierarchical porous Co_3O_4 nanowires.

4 Conclusion

In summary, 1D porous Co_3O_4 nanowires with controllable morphology and compressive strain were prepared via a facile and efficient self-template synthesis. It is critical that the introduction of ethanol in the solvent of solvothermal process is vital to the optimization of hierarchical Co_3O_4 structures and their intrinsic compressive strain. These special hierarchical porous Co_3O_4 nanowires enable the efficient oxygen evolution performance, exhibiting a low overpotential of 319 mV at 10 mA·cm^{-2} in 1 M KOH and a good stability as compared with the commercial RuO_2. Based on the complementary experimental works and DFT calculations, such excellent electrochemical performance is attributed to several features: (i) the efficient gas release and evolution as well as the effective electron and mass transfer across the porous nanowire channels; (ii) the rich exposed surface active sites, and (iii) increased electron coupling between Co-O and OH because of the proper position of d band centers of compressively strained Co_3O_4. All these studies do not only provide a good example of porous Co_3O_4 nanowire preparation but also indicate a promising method for modification of surface strain for the enhanced electrochemical performance.

Acknowledgements

This work is financially supported by the General Research Fund (CityU 11211317) and the Theme-Based Research Scheme (T42-103/16-N) of the Research Grants Council of Hong Kong SAR, China, the National Natural Science Foundation of China (No. 51672229), and the Science Technology and Innovation Committee of Shenzhen Municipality (No. JCYJ20170818095520778).

Electronic Supplementary Material: Supplementary material (SEM for PNWs, N_2 sorption isotherms, TG and FTIR figures for all the catalysts, summarized electrochemical parameters and performance comparison) is available in the online version of this article at https://doi.org/10.1007/s12274-020-2983-6.

References

[1] Suen, N. T.; Hung, S. F.; Quan, Q.; Zhang, N.; Xu, Y. J.; Chen, H. M. Electrocatalysis for the oxygen evolution reaction: Recent development and future perspectives. *Chem. Soc. Rev.* **2017**, *46*, 337–365.

[2] Seh, Z. W.; Kibsgaard, J.; Dickens, C. F.; Chorkendorff, I.; Nørskov, J. K.; Jaramillo, T. F. Combining theory and experiment in electrocatalysis: Insights into materials design. *Science* **2017**, *355*, eaad4998.

[3] Zhao, Z. J.; Liu, S. H.; Zha, S. J.; Cheng, D. F.; Studt, F.; Henkelman, G.; Gong, J. L. Theory-guided design of catalytic materials using scaling relationships and reactivity descriptors. *Nat. Rev. Mater.* **2019**, *4*, 792–804.

[4] Song, F.; Bai, L. C.; Moysiadou, A.; Lee, S.; Hu, C.; Liardet, L.; Hu, X. L. Transition metal oxides as electrocatalysts for the oxygen evolution reaction in alkaline solutions: An application-inspired renaissance. *J. Am. Chem. Soc.* **2018**, *140*, 7748–7759.

[5] Wei, Q. L.; Xiong, F. Y.; Tan, S. H.; Huang, L.; Lan, E. H.; Dunn, B.; Mai, L. Q. Porous one-dimensional nanomaterials: Design, fabrication and applications in electrochemical energy storage. *Adv. Mater.* **2017**, *29*, 1602300–1602338.

[6] Xu, C. L.; Zhao, Y. Q.; Yang, G. W.; Li, F. S.; Li, H. L. Mesoporous nanowire array architecture of manganese dioxide for electrochemical capacitor applications. *Chem. Commun.* **2009**, *48*, 7575–7577.

[7] Liu, H.; Wexler, D.; Wang, G. X. One-pot facile synthesis of iron oxide nanowires as high capacity anode materials for lithium ion batteries. *J. Alloys Compd.* **2009**, *487*, 24–27.

[8] Li, Y. G.; Tan, B.; Wu, Y. Y. Mesoporous Co_3O_4 nanowire arrays for lithium ion batteries with high capacity and rate capability. *Nano Lett.* **2008**, *8*, 265–270.

[9] Lu, X. H.; Yu, M. H.; Zhai, T.; Wang, G. M.; Xie, S. L.; Liu, T. Y.; Liang, C. L.; Tong, Y. X.; Li, Y. High energy density asymmetric quasi-solid-state supercapacitor based on porous vanadium nitride nanowire anode. *Nano Lett.* **2013**, *13*, 2628–2633.

[10] Bilousov, O. V.; Geaney, H.; Carvajal, J. J.; Zubialevich, V. Z.; Parbrook, P. J.; Giguère, A.; Drouin, D.; Díaz, F.; Aguiló, M.; O'Dwyer, C. Fabrication of p-type porous GaN on silicon and epitaxial GaN. *Appl. Phys. Lett.* **2013**, *103*, 112103–112108.

[11] Liu, H. J.; Jin, L. H.; He, P.; Wang, C. X.; Xia, Y. Y. Direct synthesis of mesoporous carbon nanowires in nanotubes using MnO_2 nanotubes as a template and their application in supercapacitors. *Chem. Commun.* **2009**, 6813–6815.

[12] Li, W.; Zhang, F.; Dou, Y. Q.; Wu, Z. X.; Liu, H. J.; Qian, X. F.; Gu, D.; Xia, Y. Y.; Tu, B.; Zhao, D. Y. A self-template strategy for the synthesis of mesoporous carbon nanofibers as advanced supercapacitor electrodes. *Adv. Energy Mater.* **2011**, *1*, 382–386.

[13] Ling, T.; Zhang, T.; Ge, B. H.; Han, L. L.; Zheng, L. R.; Lin, F.; Xu, Z. R.; Hu, W. B.; Du, X. W.; Davey, K. et al. Well-dispersed nickel- and zinc-tailored electronic structure of a transition metal oxide for highly active alkaline hydrogen evolution reaction. *Adv. Mater.* **2019**, *31*, 1807771–1807778.

[14] Ling, T.; Da, P. F.; Zheng, X. L.; Ge, B. H.; Hu, Z. P.; Wu, M. Y.; Du, X. W.; Hu, W. B.; Jaroniec, M.; Qiao, S. Z. Atomic-level structure engineering of metal oxides for high-rate oxygen intercalation pseudocapacitance. *Sci. Adv.* **2018**, *4*, eaau6261.

[15] Voiry, D.; Yamaguchi, H.; Li, J. W.; Silva, R.; Alves, D. C. B.; Fujita, T.; Chen, M. W.; Asefa, T.; Shenoy, V. B.; Eda, G. et al. Enhanced catalytic activity in strained chemically exfoliated WS_2 nanosheets for hydrogen evolution. *Nat. Mater.* **2013**, *12*, 850–855.

[16] Guan, B. Y.; Yu, X. Y.; Wu, H. B.; Lou, X. W. Complex nanostructures from materials based on metal–organic frameworks for electrochemical energy storage and conversion. *Adv. Mater.* **2017**, *29*, 1703614–1703634.

[17] Tackett, B. M.; Sheng, W. C.; Chen, J. G. Opportunities and challenges in utilizing metal-modified transition metal carbides as low-cost electrocatalysts. *Joule* **2017**, *1*, 253–263.

[18] Yu, L.; Yu, X. Y.; Lou, X. W. The design and synthesis of hollow micro-/nanostructures: Present and future trends. *Adv. Mater.* **2018**, *30*, 1800939–1800966.

[19] Luo, M. C.; Guo, S. J. Strain-controlled electrocatalysis on multimetallic nanomaterials. *Nat. Rev. Mater.* **2017**, *2*, 17059–17073.

[20] Strasser, P.; Koh, S.; Anniyev, T.; Greeley, J.; More, K.; Yu, C. F.; Liu, Z. C.; Kaya, S.; Nordlund, D.; Ogasawara, H. et al. Lattice-strain control of the activity in dealloyed core-shell fuel cell catalysts. *Nat. Chem.* **2010**, *2*, 454–460.

[21] Hammer, B.; Nørskov, J. K. Theoretical surface science and catalysis—calculations and concepts. *Adv. Catal.* **2000**, *45*, 71–129.

[22] Li, H.; Tsai, C.; Koh, A. L.; Cai, L. L.; Contryman, A. W.; Fragapane, A. H.; Zhao, J. H.; Han, H. S.; Manoharan, H. C.; Abild-Pedersen, F. et al. Activating and optimizing MoS_2 basal planes for hydrogen evolution through the formation of strained sulphur vacancies. *Nat. Mater.* **2016**, *15*, 48–53.

[23] Ling, T.; Yan, D. Y.; Wang, H.; Jiao, Y.; Hu, Z. P.; Zheng, Y.; Zheng, L. R.; Mao, J.; Liu, H.; Du, X. W. et al. Activating cobalt(II) oxide nanorods for efficient electrocatalysis by strain engineering. *Nat. Commun.* **2017**, *8*, 1509–1516.

[24] Chen, Y. B.; Li, H. Y.; Wang, J. X.; Du, Y. H.; Xi, S. B.; Sun, Y. M.; Sherburne, M.; Ager III, J. W.; Fisher, A. C.; Xu, Z. J. Exceptionally active iridium evolved from a pseudo-cubic perovskite for oxygen evolution in acid. *Nat. Commun.* **2019**, *10*, 572–582.

[25] Giannozzi, P.; Andreussi, O.; Brumme, T.; Bunau, O.; Nardelli, M, B.; Calandra, M.; Car, R.; Cavazzoni, C.; Ceresoli, D.; Cococcioni, M. et al. Advanced capabilities for materials modelling with quantum ESPRESSO. *J. Phys. Condens. Matter* **2017**, *29*, 465901–465931.

[26] Giannozzi, P.; Baroni, S.; Bonini, N.; Calandra, M.; Car, R.; Cavazzoni, C.; Ceresoli, D.; Chiarotti, G. L.; Cococcioni, M.; Dabo, I. QUANTUM ESPRESSO: A modular and open-source software project for quantum simulations of materials. *J. Phys. Condens. Matter* **2009**, *21*, 395502–395521.

[27] Perdew, J. P.; Burke, K.; Ernzerhof, M. Generalized gradient approximation made simple. *Phys. Rev. Lett.* **1996**, *77*, 3865–3868.

[28] Grimme, S.; Antony, J.; Ehrlich, S.; Krieg, H. A consistent and accurate *ab initio* parametrization of density functional dispersion correction (DFT-D) for the 94 elements H-Pu. *J. Chem. Phys.* **2010**, *132*, 154104–154119.

[29] Vanderbilt, D. Soft self-consistent pseudopotentials in a generalized eigenvalue formalism. *Phys. Rev. B* **1990**, *41*, 7892–7895.

[30] Lejaeghere, K.; Bihlmayer, G.; Björkman, T.; Blaha, P.; Blügel, S.; Blum, V.; Caliste, D.; Castelli, I. E.; Clark, S. J.; Dal Corso, A. et al. Reproducibility in density functional theory calculations of solids. *Science* **2016**, *351*, aad3000.

[31] Kaneti, Y. V.; Tang, J.; Salunkhe, R. R.; Jiang, X. C.; Yu, A. B.; Wu, K. C. W.; Yamauchi, Y. Nanoarchitectured design of porous materials and nanocomposites from metal-organic frameworks. *Adv. Mater.* **2017**, *29*, 1604898–1604938.

[32] Wei, R. J.; Fang, M.; Dong, G. F.; Lan, C. Y.; Shu, L.; Zhang, H.; Bu, X. M.; Ho, J. C. High-index faceted porous Co_3O_4 nanosheets with oxygen vacancies for highly efficient water oxidation. *ACS Appl. Mater. Interfaces* **2018**, *10*, 7079–7086.

[33] Lai, J. P.; Niu, W. X.; Luque, R.; Xu, G. B. Solvothermal synthesis of metal nanocrystals and their applications. *Nano Today* **2015**, *10*, 240–267.

[34] Wei, Q. L.; Xiong, F. Y.; Tan, S. S.; Huang, L.; Lan, E. H.; Dunn, B.; Mai, L. Q. Porous one-dimensional nanomaterials: Design, fabrication and applications in electrochemical energy storage. *Adv. Mater.* **2017**, *29*, 1602300–1602339.

[35] Ren, L.; Wang, P. P.; Han, Y. S.; Hu, C. W.; Wei, B. Q. Synthesis of $CoC_2O_4{\cdot}2H_2O$ nanorods and their thermal decomposition to Co_3O_4 nanoparticles. *Chem. Phys. Lett.* **2009**, *476*, 78–83.

[36] Hunter, B. M.; Hieringer, W.; Winkler, J. R.; Gray, H. B.; Müller, A. M. Effect of interlayer anions on [NiFe]-LDH nanosheet water oxidation activity. *Energy Environ. Sci.* **2016**, *9*, 1734–1743.

[37] Cai, Z. Y.; Bu, X. M.; Wang, P.; Ho, J. C.; Yang, J. H.; Wang, X. Y. Recent advances in layered double hydroxide electrocatalysts for the oxygen evolution reaction. *J. Mater. Chem. A* **2019**, *7*, 5069–5089.

[38] Tang, T.; Jiang, W. J.; Niu, S.; Liu, N.; Luo, H.; Chen, Y. Y.; Jin, S. F.; Gao, F.; Wan, L. J.; Hu, J. S. Electronic and morphological dual modulation of cobalt carbonate hydroxides by Mn doping toward highly efficient and stable bifunctional electrocatalysts for overall water splitting. *J. Am. Chem. Soc.* **2017**, *139*, 8320–8328.

[39] Bu, X. M.; Wei, R. J.; Gao, W.; Lan, C. Y.; Ho, J. C. A unique sandwich structure of a CoMnP/Ni_2P/NiFe electrocatalyst for highly efficient overall water splitting. *J. Mater. Chem. A* **2019**, *7*, 12325–12332.

[40] Liang, X. G.; Dong, R. T.; Li, D. P.; Bu, X. M.; Li, F. Z.; Shu, L.; Wei, R. J.; Ho, J. C. Coupling of nickel boride and $Ni(OH)_2$ nanosheets with hierarchical interconnected conductive porous structure synergizes the oxygen evolution reaction. *ChemCatChem* **2018**, *10*, 4555–4561.

[41] Anantharaj, S.; Kundu, S. Do the evaluation parameters reflect intrinsic activity of electrocatalysts in electrochemical water splitting? *ACS Energy Lett.* **2019**, *4*, 1260–1264.

[42] Lu, X. Y.; Zhao, C. Electrodeposition of hierarchically structured three-dimensional nickel-iron electrodes for efficient oxygen evolution at high current densities. *Nat. Commun.* **2015**, *6*, 6616–6623.